Verification of a Total Lagrangian ANCF Solution Procedure for Fluid–Structure Interaction Problems

Emanuele Grossi
Department of Mechanical and Industrial Engineering,
University of Illinois at Chicago,
Chicago, IL 60607
e-mail: egross20@uic.edu

Ahmed A. Shabana
Department of Mechanical and Industrial Engineering,
University of Illinois at Chicago,
Chicago, IL 60607
e-mail: shabana@uic.edu

The objective of this investigation is to verify a new total Lagrangian continuum-based fluid model that can be used to solve two- and three-dimensional fluid–structure interaction problems. Large rotations and deformations experienced by the fluid can be captured effectively using the finite element (FE) absolute nodal coordinate formulation (ANCF). ANCF elements can describe arbitrarily complex fluid shapes without imposing any restriction on the amount of rotation and deformation within the finite element, ensure continuity of the time-rate of position vector gradients at the nodal points, and lead to a constant mass matrix regardless of the magnitude of the fluid displacement. Fluid inertia forces are computed, considering the change in the fluid geometry as the result of the large displacements. In order to verify the ANCF solution, the dam-break benchmark problem is solved in the two- and three-dimensional cases. The motion of the fluid free surface is recorded before and after the impact on a vertical wall placed at the end of the dam dry deck. The results are in good agreement with those obtained by other numerical methods. The results obtained in this investigation show that the number of degrees-of-freedom (DOF) required for ANCF convergence is around one order of magnitude less than what is required by other existing methods. Limitations and advantages of the verified ANCF fluid model are discussed. [DOI: 10.1115/1.4038904]

Keywords: fluid–structure interaction, liquid sloshing, absolute nodal coordinate formulation, multibody system dynamics, dam-break problem

1 Introduction

Fluid–structure interaction is an important problem in many engineering applications. It is important to predict at the design stage the adverse effects of impact loads on maritime structures and ships, liquid oscillations in storage tanks due to earthquakes, liquid motion occurring in containers during sailing, and liquid sloshing in freight trains and highway vehicles. Most of the techniques, proposed to model fluid problems with free surface, are mainly based on the Lagrangian or Eulerian approaches. In the first approach, the fluid is represented by a finite element (FE) or finite difference mesh which coincides with and moves with the fluid material points. The governing Navier–Stokes equations of motion are simpler when a Lagrangian scheme is used because of the absence of nonlinear convection terms. Furthermore, accurate prediction of the location of the free surface is straightforward because the mesh points and nodes coincide with the fluid material points. The main shortcoming of the Lagrangian approach, however, is the loss in numerical accuracy in the case of severe mesh distortions which may require the use of an automatic remeshing algorithm, particularly in large-scale problems. In the Eulerian schemes, on the other hand, the domain under investigation is subdivided into cells which remain fixed in space while the fluid flows through them. For this reason, this formulation is more suited for the analysis of turbulent flows [1]. However, since the mapping between Eulerian mesh and fluid material points is lost, additional effort is needed to accurately capture the location of the free surface. The marker and cell method [2–6] and the volume of fluid method [7–11] are the most popular techniques used to recognize the region occupied by the fluid. The marker and cell method uses virtual particles to track the fluid position [2,3,12]. The volume of fluid method, proposed by Hirt and Nichols [7], introduces an auxiliary function F which assumes the value 1 in the fluid region and 0 anywhere else. An additional equation, $\partial F/\partial t + \mathbf{v} \cdot \nabla F = 0$, must be solved to study the time evolution of F, where $\mathbf{v}$ is the fluid velocity vector.

To combine the advantages of Lagrangian and Eulerian schemes, the arbitrary Lagrangian Eulerian (ALE) methods have been proposed. In the ALE formulations, the motions of the mesh and the material points are both described. A major feature of this hybrid method is the appearance of convection terms in the momentum and continuity equations. ALE methods have been widely used in the solution of viscous, free surface problems [13–17]. For additional details on the ALE method, the reader can refer to Belytschko et al. [18].

In the last decades, a fully Lagrangian meshless technique called smoothed particle hydrodynamics (SPH) was introduced to study fluid dynamic problems [19–31]. In general, mesh-free methods adopt scattered data interpolation techniques, among which the moving least squares interpolation is the most popular [32]. SPH techniques, similar to Eulerian methods, can describe very complex fluid scenarios including turbulent and multiphase flows.

The level of difficulty in the analysis of fluid dynamics problems increases considerably if liquid motion occurs inside containers which are components of complex mechanical systems, such as vehicles, rockets, and aircrafts. The Federal Motor Carrier Safety Administration (FMCSA) has recently conducted computer simulations and driving experiments on single-unit trucks carrying intermediate bulk containers (IBCs) half-filled with water [33]. For this investigation, the commercial software TRUCKSIM was used. In case of moderate sloshing scenarios, the fluid motion in the TRUCKSIM model was represented by discrete inertia models used to account for the effect of the liquid sloshing oscillations. However, the integration of the TRUCKSIM vehicle model with a

Manuscript received July 12, 2017; final manuscript received December 18, 2017; published online February 12, 2018. Assoc. Editor: Christopher J. Freitas.

computational fluid dynamics (CFD) continuum-based liquid model was not achieved due to the high level of complexity of this task. Cheli et al. [34] studied the interaction between fluid sloshing and vehicle dynamics. The fluid/tank system was modeled in the commercial CFD software FLUENT, and a simple 14 DOFs rigid vehicle model was introduced using a user subroutine. However, this approach does not allow for the implementation of complex vehicle models which include flexible and highly nonlinear components like tires and leaf springs.

A possible solution for the integration of liquid and complex mechanical system models is to use a cosimulation approach, which requires two or more solvers to run at the same time and exchange information at predefined time steps. Elliot et al. [35] employed a cosimulation approach in which the explicit CFD code Dytran and the implicit multibody system (MBS) dynamics solver ADAMS are used, while Barton at al. [36] used a similar approach by establishing a link between the CFD solver ACUSOLVE and the MBS software MOTIONSOLVE. However, the development of credible cosimulation models can be very challenging in some applications because of the difficulty of establishing efficient communications between different algorithms and software that are based on fundamentally different approaches, the challenges in capturing highly nonlinear effects including centrifugal and Coriolis forces that characterize the motion of mechanical systems such as vehicles, and the very high computational cost as the result of using some of the existing methods that require the use of very large number of degrees-of-freedom (DOF).

Compared to the Eulerian approach, the fluid dynamic community has shown less interest in using the total Lagrangian continuum-based methods for the analysis of fluid–structure interaction problems. A description of the fluid behavior using a total Lagrangian approach allows for a systematic integration with vehicle models developed using MBS algorithms, which are widely used both in industry and academia for the analysis of complex mechanical systems. Wei et al. [37] developed a total Lagrangian nonincremental liquid sloshing model based on the FE absolute nodal coordinate formulation (ANCF). This solution procedure was systematically integrated by Shi et al. [38] with a complex railroad vehicle model and by Nicolsen at al. [39] with a fully nonlinear truck model. Nonetheless, the ANCF fluid models which can be effectively used to model liquid sloshing in very complex vehicle motion scenarios have not been validated. ANCF finite elements can describe an arbitrarily large displacement including large rigid body translations and rotations, and therefore, such elements are ideally suited for the integration of fluid models with complex mechanical system models.

The main goal of this paper is to verify the total Lagrangian ANCF finite element liquid sloshing model presented by Wei et al. [37] by comparing the results of this model with numerical and experimental results published in the literature. The dam-break is a benchmark problem widely used to assess the performance of numerical schemes in fluid–structure interaction problems [8,20,40–48]. In this paper, the broken dam problem is solved both in the two- and three-dimensional cases. This paper makes the following specific contributions:

(1) It is explained how ANCF finite elements can be used to develop a total Lagrangian continuum-based formulation that is suited for the analysis of the dam-break problem. Both two- and three-dimensional fluid motion scenarios will be considered in this study. For the planar analysis, the ANCF rectangular element is used, while the solid element is used for the spatial analysis. Both ANCF finite elements used in this investigation ensure the continuity of the gradient vectors and their time derivative at the nodal points. Consequently, the time rate of the gradient vectors that enter into the formulation of the Navier–Stokes equations are continuous at the nodal points.
(2) The results obtained using the total Lagrangian formulation based on the ANCF finite elements are verified by comparing with experimental and numerical results published in the literature. It is shown that, because ANCF finite elements can describe complex geometric shapes, models with significantly less number of degrees-of-freedom can be developed. The verification of the ANCF models using published results is necessary in order to be able to use such a new approach with confidence in the future to study liquid sloshing in complex motion scenarios that are encountered in highway, rail, marine, and aerospace applications.
(3) The advantages and limitations of the total Lagrangian formulation based on ANCF finite elements in the analysis of fluid–structure interaction problems are identified in order to define the scope of the applicability of the new total Lagrangian approach.

The paper is organized as follows. In Sec. 2, the dam-break problem used in this investigation is described and a general overview of the solution procedure is outlined. The ANCF constitutive equations are described in Sec. 3. Sections 4 and 5 describe the governing equations and boundary conditions, while Secs. 6 and 7 present the numerical results of the broken dam problem for the two- and three-dimensional cases. Section 8 discusses the advantages and disadvantages of the total Lagrangian ANCF fluid approach and compares it with the most popular numerical methods employed in the fluid dynamics research. Section 9 presents a summary and the main conclusions drawn from this study.

2 Study Model

The fluid flow generated after the breaking of a dam is studied, reproducing the experiment carried out by Martin and Moyce [49]. In the experiment, the fluid is chosen as water which is assumed to have mass density $\rho = 1000\,\mathrm{kg/m^3}$, and viscosity $\nu_v = 10^{-3}$ Pa·s. A diagram of the experimental apparatus which was used is shown in Fig. 1. In the initial configuration, the fluid is assumed to be in hydrostatic equilibrium, confined on three sides by rigid walls and on the front side by a piece of wax paper. The initial fluid geometric shape is a cube with sides that have length $H = 0.05715\,\mathrm{m}$. A short circuit in the system causes the wax paper to melt and the column of water collapses over a dry deck under the effect of gravity. In this investigation, the gravity constant is $g = 9.81\,\mathrm{m/s^2}$.

Numerical simulations are performed to accurately capture the fluid free surface shape and the position of the water front. The problem is studied at the early stage after the dam break in order to be able to compare the obtained results with the experimental and numerical data available from the literature. The effect of aerodynamic forces and turbulence are neglected. The problem is analyzed both in the two-dimensional and three-dimensional cases. The Navier–Stokes equations are used to formulate the viscosity forces and the fluid partial differential equations of motion are reduced to a set of discrete second-order ordinary differential equations by applying the principle of virtual work and approximating the displacement field using the ANCF finite element kinematic description. The initial nodal coordinates are known from the problem geometry, and the initial nodal velocities are assumed to be zeros. The dam is modeled as a rigid body, because it does not undergo any deformation, and frictionless contact boundary conditions are applied at the outer fluid surface. The fluid equations of motion are integrated numerically using the implicit Hilber–Hughes–Taylor (HHT) algorithm. At each time-step, the fluid stress tensor is computed using the fluid constitutive laws and used with the Green–Lagrange strain tensor to formulate the fluid viscous forces. The fluid incompressibility condition is ensured by using a penalty method. When ANCF finite elements are used, the mass matrix is always constant regardless of the magnitude of the displacement. As a result, the inertia forces do not have quadratic velocity terms as will be explained in this paper. The change in the fluid accelerations due to the continuous

deformation can then be accurately predicted and used to formulate the generalized fluid inertia forces. Penetration between the fluid and the dam walls is prevented using a penalty contact algorithm which efficiently detects the contact regions.

3 ANCF Fluid Constitutive Model

In this section, the general ANCF fluid constitutive model is described. In the ANCF description, the vector of the element nodal coordinates consists of absolute position and gradient vectors. Using the gradient vectors as nodal coordinates, the ANCF displacement field can describe an arbitrarily large displacement as well as complex fluid geometry [50]. The fluid is assumed to be Newtonian and incompressible, viscosity is assumed to be constant, and the effect of temperature is neglected. In the most general case, the fluid behavior can be described using three different configurations, namely the straight, reference, and current configurations (see Fig. 2). The use of these configurations allows describing systematically the initial fluid geometry that can assume the shape of the container. Let V, V_0, and v be the fluid volumes in the three configurations and $\mathbf{x}$, $\mathbf{X}$, and $\mathbf{r}$ be the associated position vectors of an arbitrary point on the fluid. For a general ANCF element j, the position vector of an arbitrary point defined in the reference and current configurations are written, respectively, as $\mathbf{X}^j = [\,X^j \quad Y^j \quad Z^j\,]^{\mathrm{T}} = \mathbf{S}^j\mathbf{e}_0^j$ and $\mathbf{r}^j = \mathbf{S}^j\mathbf{e}^j$, where $\mathbf{S}^j$ is the shape function matrix, $\mathbf{e}_0^j$ and $\mathbf{e}^j$ are the element nodal coordinates in the reference and current configurations, respectively [50]. The relation between the volumes in the reference and current configurations can be expressed as $dv^j = J^j dV_0^j$, where J^j is the determinant of the matrix of position vector gradients $\mathbf{J}^j = \partial\mathbf{r}^j/\partial\mathbf{X}^j$. It is easier to perform the integration over the volume in the reference configuration instead of the volume in the current configuration, because the geometry at the beginning of the simulation is known. In general, the reference configuration can be curved, therefore integration can be further simplified by introducing a straight reference configuration, which can be systematically obtained from the reference configuration using the relationship $dV_0^j = J_0^j dV^j$, where $\mathbf{J}_0^j = \partial\mathbf{X}^j/\partial\mathbf{x}^j$ is a constant Jacobian matrix. The mapping between the current and straight configuration is defined by $\mathbf{J}_e^j = \partial\mathbf{r}^j/\partial\mathbf{x}^j$ and leads to the relation $dv^j = J_e^j dV^j$. One can show that $\mathbf{J}^j = \partial\mathbf{r}^j/\partial\mathbf{X}^j = (\partial\mathbf{r}^j/\partial\mathbf{x}^j)(\partial\mathbf{x}^j/\partial\mathbf{X}^j) = \mathbf{J}_e^j\mathbf{J}_0^{j^{-1}}$. In the problem considered in this investigation, the elements in the reference configuration are straight, and consequently, the mapping between the reference and straight configurations $\mathbf{J}_0^j$ is the identity matrix.

The Cauchy stress tensor can be written as the sum of its isotropic and deviatoric parts as $\boldsymbol{\sigma} = -p\mathbf{I} + \mathbf{S}_\sigma$, where p is the fluid hydrostatic pressure defined as $p = -1/3\mathrm{tr}(\boldsymbol{\sigma})$, and $\mathbf{S}_\sigma = (S_{ij})$ is the symmetric stress deviator tensor which has zero trace and accounts for shear effects. In case of a Newtonian fluid, the components of the stress deviator tensor depend linearly on the velocity gradients, that is, $S_{ij} = A_{ijkl}(\partial v_k/\partial r_l)$, where A_{ijkl} is a fourth-order tensor. In case of an isotropic Newtonian fluid, it possible to prove that $\mathbf{S}_\sigma = \lambda\mathrm{tr}(\mathbf{D})\mathbf{I} + 2\mu\mathbf{D}$, where $\mathbf{D} = (1/2)(\mathbf{L} + \mathbf{L}^{\mathrm{T}})$ is the rate of deformation tensor, $\mathbf{L} = \partial\mathbf{v}/\partial\mathbf{r}$ is the tensor of velocity vector gradients, λ is the Lame's constant, μ is the coefficient of dynamic viscosity, and $(\lambda + (2\mu/3))$ is the coefficient of Bulk viscosity. The final fluid constitutive equation for a Newtonian isotropic fluid can be written as $\boldsymbol{\sigma} = [-p + \lambda\mathrm{tr}(\mathbf{D})]\mathbf{I} + 2\mu\mathbf{D}$. If $\lambda + (2\mu/3) = 0$, one has the *Stokes' relation*. In the most general case λ, μ, and p are functions of both density and temperature.

4 Governing Equations

The fluid partial differential equations of equilibrium are given by $(\nabla\cdot\boldsymbol{\sigma}^{\mathrm{T}})^{\mathrm{T}} + \mathbf{f}_b - \rho\mathbf{a} = \mathbf{0}$, where $\boldsymbol{\sigma}$ is the Cauchy stress tensor, $\mathbf{f}_b$ is the vector of body forces, ρ is the mass density, and $\mathbf{a}$ is the absolute acceleration vector. The fluid continuity equation $(\partial\rho(\mathbf{r},t)/\partial t) + \nabla\cdot(\rho\mathbf{v}) = 0$ is reduced to $\nabla\cdot\mathbf{v} = 0$ in the case of incompressible materials. Substituting the expression of the stress tensor defined in Sec. 3 and considering the incompressibility condition, one obtains the incompressible Navier–Stokes formulation defined by the two equations

$$\rho\mathbf{a} = \mathbf{f}_b + \{-\nabla\cdot(p\mathbf{I}) + \lambda\nabla\cdot(\mathrm{tr}(\mathbf{D})\mathbf{I}) + 2\mu\nabla\cdot\mathbf{D}\}^{\mathrm{T}}, \quad \nabla\cdot\mathbf{v} = 0 \tag{1}$$

Obtaining an accurate and stable solution of incompressible fluids is a very challenging task. The most popular solution strategies in the literature can be classified as the *pressure stabilization techniques*, *penalty methods*, *artificial compressibility methods*, and *operator splitting techniques* [51]. In an Eulerian description, a common source of instability in the solution of the fluid equations comes from the strong nonlinearity associated with the convective term of the acceleration vector, defined as $\mathbf{a} = D\mathbf{v}(\mathbf{r},t)/Dt = (\partial\mathbf{v}(\mathbf{r},t)/\partial t) + \mathbf{v}\cdot\nabla\mathbf{v}$ [52]. If a Lagrangian approach is used, the velocity vector is directly a function of the material coordinates, therefore, the acceleration vector can be written simply as $\mathbf{a} = d\mathbf{v}(\mathbf{X},t)/dt$ with $\mathbf{v} = d\mathbf{r}/dt$, simplifying considerably the numerical calculations. In the case of ANCF elements, the absolute velocity and acceleration vectors of an arbitrary point on an element j are simply given by $\mathbf{v}^j = \mathbf{S}^j\dot{\mathbf{e}}^j$ and $\mathbf{a}^j = \mathbf{S}^j\ddot{\mathbf{e}}^j$, respectively.

In this paper, the principle of virtual work and the ANCF displacement field are used to determine a set of discrete ordinary differential equations that govern the dynamics of the continuum as

$$\mathbf{M}^j\ddot{\mathbf{e}}^j = \mathbf{Q}_b^j + \mathbf{Q}_t^j + \mathbf{Q}_C^j - \mathbf{Q}_P^j + \mathbf{Q}_v^j \tag{2}$$

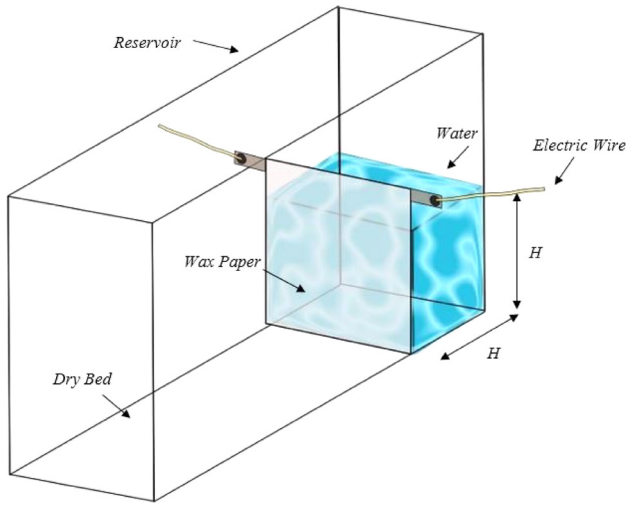

Fig. 1 Experiment (H = 0.05715 m)

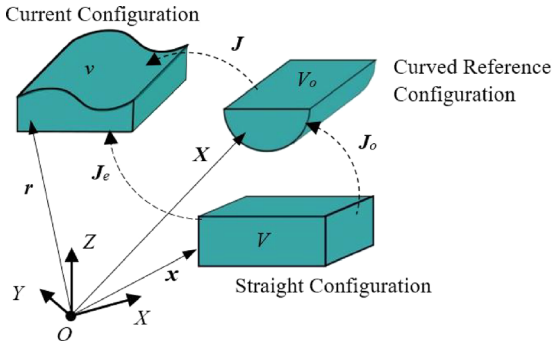

Fig. 2 The three general fluid configurations

where $\mathbf{M}^j$ is the constant symmetric mass matrix of the element, $\mathbf{Q}_b^j$ and $\mathbf{Q}_t^j$ are the vectors of generalized body and surface traction forces, $\mathbf{Q}_C^j$ is the vector of generalized contact forces, $\mathbf{Q}_v^j$ is the vector of generalized viscous forces, and $\mathbf{Q}_P^j$ is the vector of generalized penalty forces. A flowchart of the numerical solution procedure is shown in Fig. 3. The time-step and tolerance selected to obtain convergence of the results are, respectively, $\Delta t = 0.00015$ s and tol $= 10^{-8}$.

4.1 Viscous Forces. In case of an incompressible fluid, $\nabla \cdot \mathbf{v} = \text{tr}(\mathbf{D}) = 0$, and the expression of the Cauchy stress tensor derived in Sec. 3 reduces to

$$\boldsymbol{\sigma}^j = -p^j \mathbf{I} + 2\mu \mathbf{D}^j \tag{3}$$

The first term on the right-hand side of Eq. (3) is associated with volumetric forces, while the second term is related to viscous forces. The integration of the equations of motion over the reference domain requires using consistent stress and strain definitions, namely the second Piola–Kirchhoff stress tensor $\boldsymbol{\sigma}_{P2}$ and the Green–Lagrange strain tensor $\boldsymbol{\varepsilon}$. The virtual work of the fluid viscous forces can be written in the reference configuration as

$$\delta W_v^j = -\int_{v^j} \boldsymbol{\sigma}^j : (\delta \mathbf{J}^j)(\mathbf{J}^j)^{-1} dv = -\int_{V_0^j} \boldsymbol{\sigma}_{P2}^j : \delta \boldsymbol{\varepsilon}^j dV_0^j \tag{4}$$

where $\boldsymbol{\varepsilon}^j = (\mathbf{J}^{\mathrm{T}}\mathbf{J}^j - \mathbf{I})/2$ and $\boldsymbol{\sigma}_{P2}^j = J^j(\mathbf{J}^j)^{-1} 2\mu \mathbf{D}^j (\mathbf{J}^j)^{-1^{\mathrm{T}}}$. Using the kinematic relationship $\mathbf{D}^j = (\mathbf{J}^j)^{-1^{\mathrm{T}}} \dot{\boldsymbol{\varepsilon}}^j (\mathbf{J}^j)^{-1}$, one has

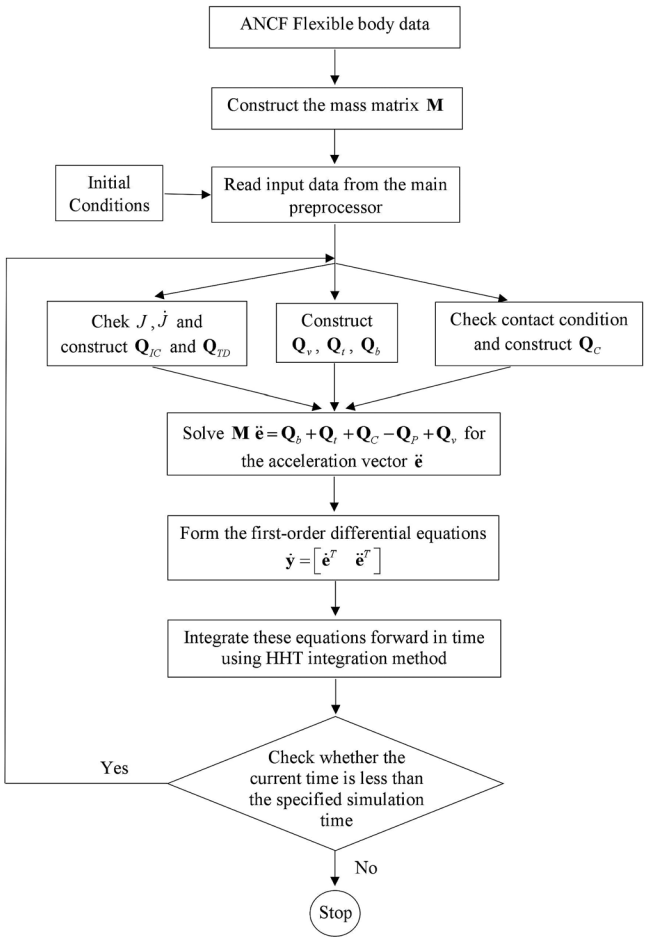

Fig. 3 Flowchart of the numerical solution procedure

$$\begin{aligned}\delta W_v^j &= -\int_{V_0^j} J^j (\mathbf{J}^j)^{-1} 2\mu (\mathbf{J}^j)^{-1^{\mathrm{T}}} \dot{\boldsymbol{\varepsilon}}^j (\mathbf{J}^j)^{-1} (\mathbf{J}^j)^{-1^{\mathrm{T}}} : \delta \boldsymbol{\varepsilon}^j dV_0^j \\ &= -\int_{V_0^j} 2\mu J^j (\mathbf{C}_r^j)^{-1} \dot{\boldsymbol{\varepsilon}} (\mathbf{C}_r^j)^{-1} : \delta \boldsymbol{\varepsilon}^j dV_0^j \end{aligned} \tag{5}$$

where $\mathbf{C}_r^j = (\mathbf{J}^j)^{\mathrm{T}} \mathbf{J}^j$ is the right Cauchy–Green deformation tensor. Using the virtual change in the strains $\delta \boldsymbol{\varepsilon}^j = (\partial \boldsymbol{\varepsilon}^j / \partial \mathbf{e}^j) \delta \mathbf{e}^j$, the generalized viscous forces associated with the ANCF nodal coordinates can be written as

$$\mathbf{Q}_v^j = -\int_{V_0^j} 2\mu J^j \left[(\mathbf{C}_r^j)^{-1} \dot{\boldsymbol{\varepsilon}} (\mathbf{C}_r^j)^{-1} \right] : \frac{\partial \boldsymbol{\varepsilon}^j}{\partial \mathbf{e}^j} dV_0^j \tag{6}$$

The viscosity forces of this equation are evaluated using numerical integration methods.

4.2 Incompressibility Condition. For an incompressible material, $dv = J dV_0$, and the determinant of the matrix of position vector gradients J is constant and equal to one. One method to enforce the incompressibility condition is to add, to the system differential equations of motion, the algebraic constraint equation $J = 1$, which must be satisfied at the position, velocity, and acceleration levels everywhere in the continuum. However, in the numerical implementation, it is more efficient and simpler to use a penalty approach to enforce the incompressibility condition. For a finite element j, the constraint $J^j = 1$ is enforced by introducing the penalty strain energy function $U_{IC}^j = (1/2) k_{IC}^j (J^j - 1)^2$, where k_{IC}^j is a penalty coefficient selected to ensure that the condition $J = 1$ is satisfied to within acceptable tolerance. The corresponding vector of generalized penalty forces associated with the ANCF nodal coordinates is obtained by differentiating U_{IC}^j with respect to the nodal coordinates of the element j as $\mathbf{Q}_{IC}^j = \partial U_{IC}^j / \partial \mathbf{e}^j = k_{IC}^j (J^j - 1) \partial J^j / \partial \mathbf{e}^j$. In order to satisfy the isochoric constraint at the velocity level, the dissipation function $U_{TD}^j = (1/2) c_{TD}^j (\dot{J}^j)^2$ is used, where c_{TD}^j is a penalty damping coefficient. The associated damping penalty forces can also be written as $\mathbf{Q}_{TD}^j = \partial U_{TD}^j / \partial \dot{\mathbf{e}}^j = c_{TD}^j \dot{J}^j (\partial \dot{J}^j / \partial \dot{\mathbf{e}}^j)$, where $\dot{J}^j = \text{tr}(\dot{\mathbf{D}}^j) J^j$ and $\partial \dot{J}^j / \partial \dot{\mathbf{e}}^j = \partial J^j / \partial \mathbf{e}^j$. In the two-dimensional case $J^j = (r_X^j)_1 (r_Y^j)_2 - (r_Y^j)_1 (r_X^j)_2$, where $\mathbf{r}_X^j = [\,(r_X^j)_1 \quad (r_X^j)_2\,]^{\mathrm{T}}$ and $\mathbf{r}_Y^j = [\,(r_Y^j)_1 \quad (r_Y^j)_2\,]^{\mathrm{T}}$ are the first and second columns of the matrix $\mathbf{J}^j$, respectively. One can show that

$$\left(\frac{\partial J^j}{\partial \mathbf{e}^j}\right) = \left(\frac{\partial \dot{J}^j}{\partial \dot{\mathbf{e}}^j}\right) = \mathbf{S}_{1X}^j (r_Y)_2 + \mathbf{S}_{2Y}^j (r_X)_1 - \mathbf{S}_{1Y}^j (r_X)_2 - \mathbf{S}_{2X}^j (r_Y)_1 \tag{7}$$

where $\mathbf{S}_{1X}^j$, $\mathbf{S}_{2X}^j$ and $\mathbf{S}_{1Y}^j$, $\mathbf{S}_{2Y}^j$ are the first and second rows of the derivative of the shape function matrix $\mathbf{S}^j$ with respect to X and Y coordinates, respectively. In the three-dimensional case, $J^j = \mathbf{r}_X^j \cdot (\mathbf{r}_Y^j \times \mathbf{r}_Z^j) = \mathbf{r}_Y^j \cdot (\mathbf{r}_Z^j \times \mathbf{r}_X^j) = \mathbf{r}_Z^j \cdot (\mathbf{r}_X^j \times \mathbf{r}_Y^j)$, and therefore, $\partial J^j / \partial \mathbf{e}^j$ can be written as

$$\left(\frac{\partial J^j}{\partial \mathbf{e}^j}\right) = \left(\frac{\partial \dot{J}^j}{\partial \dot{\mathbf{e}}^j}\right) = \mathbf{S}_X^{j^{\mathrm{T}}} \left(\mathbf{r}_Y^j \times \mathbf{r}_Z^j\right) + \mathbf{S}_Y^{j^{\mathrm{T}}} \left(\mathbf{r}_Z^j \times \mathbf{r}_X^j\right) + \mathbf{S}_Z^{j^{\mathrm{T}}} \left(\mathbf{r}_X^j \times \mathbf{r}_Y^j\right) \tag{8}$$

This equation shows that if $\partial J^j / \partial \mathbf{e}^j$ is known, there is no need for the differentiation $\partial \dot{J}^j / \partial \dot{\mathbf{e}}^j$.

The vector of generalized penalty forces of the fluid element j can then be written as

$$\mathbf{Q}_P^j = \mathbf{Q}_{IC}^j + \mathbf{Q}_{TD}^j \tag{9}$$

These generalized penalty forces, which are associated with the ANCF nodal coordinates, are used in the fluid equations of motion previously presented in this paper.

4.3 Inertia Forces. The use of the ANCF finite element formulation allows to systematically account for the effect of the distributed fluid inertia. The ANCF acceleration vector $\mathbf{a}^j$ can be written as $\mathbf{a}^j = \ddot{\mathbf{r}}^j = \mathbf{S}^j\ddot{\mathbf{e}}^j$, $j = 1, 2, 3, \ldots, n_e$, where n_e is the total number of ANCF elements. The virtual work of the inertia forces can be defined in the current configuration as $\delta W_i^j = \int_{v^j} \rho^j \mathbf{a}^{j\mathrm{T}} \delta\mathbf{r}^j dv^j$, where $\delta\mathbf{r}^j = \mathbf{S}^j\delta\mathbf{e}^j$. Using these two equations, the virtual work of the inertia forces can be written as

$$\delta W_i^j = \left\{ \ddot{\mathbf{e}}^{j\mathrm{T}} \int_{V_0^j} \rho_0^j \mathbf{S}^{j\mathrm{T}} \mathbf{S}^j dV_0^j \right\} \delta\mathbf{e}^j = \{\ddot{\mathbf{e}}^{j\mathrm{T}} \mathbf{M}^j\}\delta\mathbf{e}^j = \mathbf{Q}_i^{j\mathrm{T}}\delta\mathbf{e}^j \quad (10)$$

where $\mathbf{M}^j$ is the constant symmetric mass matrix of the ANCF finite element j, and $\mathbf{Q}_i^j = \mathbf{M}^j\ddot{\mathbf{e}}^j$ is the generalized inertia forces associated with the ANCF nodal coordinates.

5 Boundary Conditions

In the model considered in this study, the fluid is subjected to boundary forces that prevent the fluid from penetrating the ground and the dam walls. In order to model these forces, a contact formulation based on the penalty approach is developed. In addition to the fact that the contact forces change as a function of the fluid displacement, the region of the boundary surface which is in contact with the fluid must be determined; the resulting problem is referred to as *boundary nonlinearity* [53]. In this study, the dam is treated as a rigid body with no friction on the solid wall boundaries; an assumption often made in the literature [6,46,54–57]. The detection of the points of contact between the fluid and the boundary and the definition of the contact forces are discussed in this section.

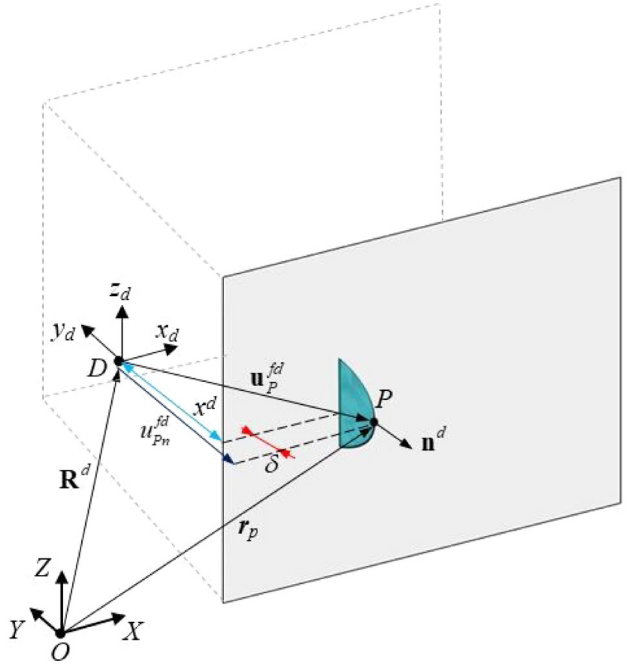

Fig. 4 Example of lateral interpenetration between the fluid and the dam wall (penetration is magnified)

The position of a potential contact point P on the outer surface of an ANCF fluid element j can be written as $\mathbf{r}_P^j = \mathbf{S}_P^j\mathbf{e}^j$, where $\mathbf{S}_P^j$ is the shape function matrix evaluated at point P. The global position of the dam reference point D is denoted as $\mathbf{R}^d$. The relative position and velocity vectors of a fluid particle with respect to the dam reference point can be written, respectively, as $\mathbf{u}_P^{fd} = \mathbf{S}_P^j\mathbf{e}^j - \mathbf{R}^d$ and $\dot{\mathbf{u}}_P^{fd} = \mathbf{S}_P^j\dot{\mathbf{e}}^j - \dot{\mathbf{R}}^d$, where $\dot{\mathbf{e}}^j$ is the vector of element nodal velocities. Because the dam is assumed to be fixed in space, $\dot{\mathbf{R}}^d = 0$. The penetration δ is defined as $\delta = u_{Pn}^{fd} - x^d$, where $u_{Pn}^{fd} = \mathbf{u}_P^{fd} \cdot \mathbf{n}^d$, $\mathbf{n}^d$ is a unit vector normal to the contact surface, and x^d a distance that defines the dam geometric boundaries. Figure 4 shows a simple illustration of lateral interpenetration between the fluid and a dam wall. If there is a penetration, the penetration and its time-rate, $\dot{\delta} = \dot{\mathbf{u}}_P^{fd} \cdot \mathbf{n}^d$, are used to evaluate the magnitude of the normal and tangential contact forces, which are defined, respectively, as $f_n = k_P\delta + C_P|\delta|\dot{\delta}$ and $f_t = \mu_f f_n$, where k_P and C_P are penalty stiffness and damping coefficients [58], and μ_f is the friction coefficient between the fluid and the dam walls. In general, the penalty force vector can be written as $\mathbf{F}_P = f_n\mathbf{n}^d - f_t\mathbf{t}^d$, where $\mathbf{t}^d$ is a unit vector in the direction of the tangential relative velocity vector $\mathbf{v}_t = \dot{\mathbf{u}}_P^{fd} - (\dot{\mathbf{u}}_P^{fd} \cdot \mathbf{n}^d)\mathbf{n}^d$. The virtual work of the penalty contact forces can be expressed as $\delta W_P = \mathbf{F}_P^{\mathrm{T}}(\delta\mathbf{r}_P^j - \delta\mathbf{r}^d)$, where $\mathbf{r}^d$ is the contact point on the dam. Because the dam is assumed to be fixed, $\delta\mathbf{r}^d = 0$, and the vector of generalized penalty forces associated with the fluid ANCF coordinates is $\mathbf{Q}_C^j = \mathbf{S}^{j\mathrm{T}}\mathbf{F}_P$. The reaction forces on the dam can also be systematically calculated, and the vector of generalized contact forces $\mathbf{Q}_C^j$ can be introduced to the right-hand side of the equations of motion.

6 Two-Dimensional Broken-Dam Flow

In the planar analysis used in this study, rectangular ANCF elements that ensure the continuity of the time-rate of the position vector gradients are used to model the broken dam problem. These elements, introduced by Olshevskiy et al. [59], are of the isoparametric type. Each element has four nodes, 24 DOFs, and cubic shape functions. As shown in Appendix A of this paper, the vector of nodal coordinates of a finite element j at a node k can be written as

$$\mathbf{e}^j = [\,\mathbf{r}^{jk\mathrm{T}} \quad \mathbf{r}_{x1}^{jk\mathrm{T}} \quad \mathbf{r}_{x2}^{jk\mathrm{T}}\,]^{\mathrm{T}}, \quad k = 1, \ldots, 4 \quad (11)$$

where $\mathbf{r}^{jk}$ is the absolute position vector of node k of element j, and $\mathbf{r}_{xl}^{jk}$ is the position gradient vector obtained by differentiation of the position vector with respect to the spatial coordinates x_l, $l = 1, 2$, with $x_1 = x$ and $x_2 = y$. Using gradients as nodal coordinates and having a high order of interpolation in the shape functions allows capturing complex fluid deformed shapes with a small number of finite elements. Figure 5 shows the effect of mesh refinement on the description of the fluid free surface at a given time instant after the breaking of the dam.

6.1 Numerical Results. The broken dam problem was solved using different numbers of elements; in this numerical investigation 9-, 16-, 64- and 100-element meshes are used. The location of the water front is measured in the early stage of the dam break problem in the case of the four models with different numbers of elements. Numerical results and mesh convergence are presented in Fig. 6 in terms of the dimensionless time and position coordinates $t^* = t\sqrt{g/H}$ and $x^* = x/H$. The free surface profiles obtained with a uniform 10×10 element mesh are shown in Fig. 7. It is clear that a relatively small number of rectangular ANCF elements is sufficient to accurately describe the free surface shape. In this investigation, the broken dam problem is solved using a uniform grid refinement. As an alternative, it is also possible to

adopt a nonuniform mesh refinement scheme by using more elements in the regions of the fluid where a large variation of the free surface geometry occurs. An example of nonuniform 10×10 element mesh is shown in Fig. 8 where a wall is placed at a distance A with respect to the water front, and the evolution of the fluid deformed shape before and after the collision with the right wall is recorded. Figure 8 shows a qualitative comparison between the fluid free surface evolution determined using the ANCF analysis and the experimental measurements of Lobovský et al. [60].

6.2 Velocity Field. Accurate description of the fluid velocity field is an essential part in the solution of the fluid dynamic problems. While Eulerian methods employ the velocity field $\mathbf{v}(\mathbf{r}, t)$ as the main kinematic variable, in the Lagrangian approach, the focus is primarily on the displacement field $\mathbf{u}(\mathbf{r}, t)$ and the expression of the absolute velocity at each point is obtained as the time derivative of the displacement. In case of the ANCF finite elements, the velocity field of an element j is obtained as $\mathbf{v}^j(\mathbf{r}, t) = \mathbf{S}^j(\mathbf{X})\dot{\mathbf{e}}^j(t)$, where $\mathbf{S}^j$ is the same shape function matrix used for the displacement interpolation. The velocity field is plotted at various time instants before the collision in Fig. 9 for the uniform 10×10 element mesh case. It is clear from the results presented in this figure that the ANCF rectangular elements can successfully capture the fluid velocity field and satisfy the velocity continuity conditions at the element nodal points.

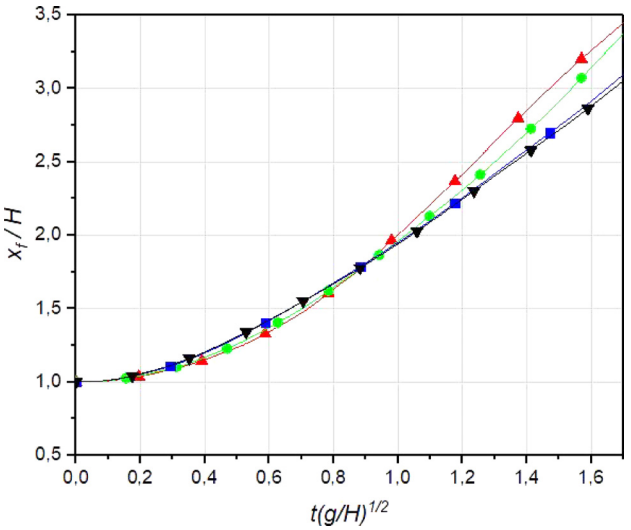

Fig. 6 Water front evolution in time predicted using rectangular ANCF elements (9 Elements, 16 Elements, 64 Elements, 100 Elements)

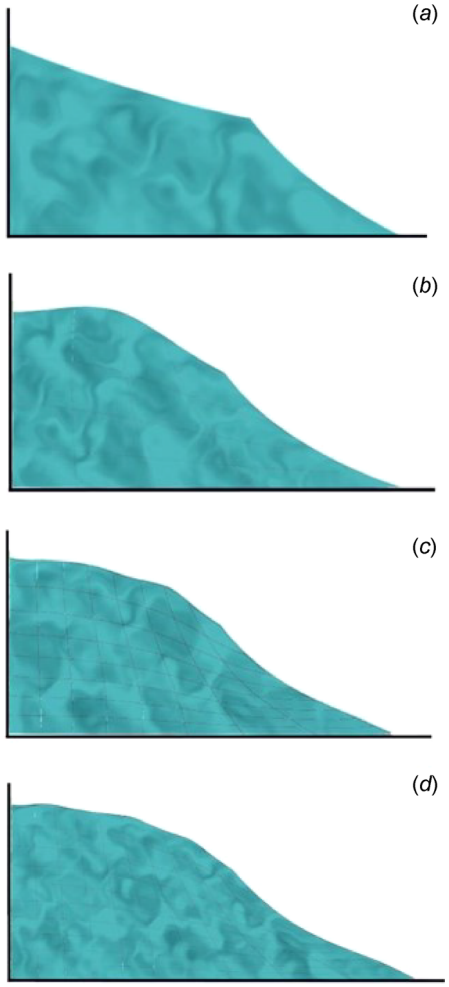

Fig. 5 Fluid deformed shape at $t = 0.08s$ for different mesh refinements: (*a*) 1, (*b*) 16, (*c*) 64, and (*d*) 100 elements

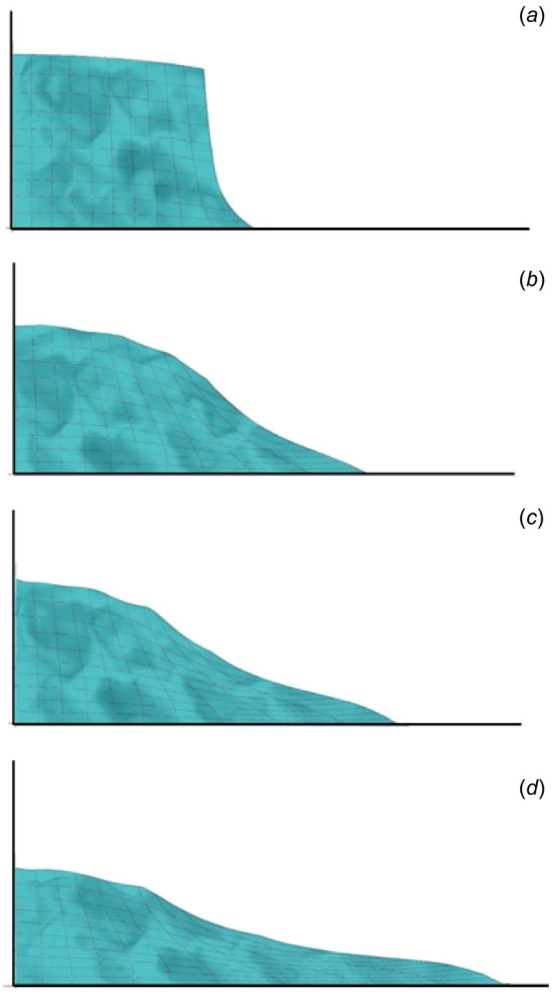

Fig. 7 Free surface profiles for the broken dam problem predicted using 100 planar elements: (*a*) 0.04 s, (*b*) 0.08 s, (*c*) 0.10 s, and (*d*) 0.13 s

6.3 Verification of the Results. The numerical results obtained in this paper are verified against experimental measurements and simulation results obtained using other methods published in the literature. The most popular methods used in the literature for the solution of the broken dam problem are the *level-set methods*, *boundary element methods* (BEM), SPH, *finite volume methods* (FVM), and *Eulerian finite element methods* (FEM). The level-set methods are computational techniques introduced by Osher and Sethian [61] to address complex problems related to fluid interface motion. The boundary element methods are widely used numerical methods for partial differential equations. Compared to the FEM and the finite difference method, BEM has the main advantage of making the discretization on a reduced domain; for a three-dimensional problem, only the surface is discretized, and in the two-dimensional case, the discretization is performed only on the boundary contour [62]. The SPH method is a fully Lagrangian mesh-less technique successfully used in a variety of fluid-dynamic problems involving complex flow fields. The finite volume scheme is an Eulerian-based method introduced in the beginning of the seventies [63,64]. The spatial domain is decomposed into control volumes, and unknown values and derivatives are obtained by interpolating nodal values. An Eulerian FVM is implemented in FLUENT, a CFD solver widely used in industry and academia [65].

An interesting comparison between the existing numerical methods and the experimental results for the broken dam problem is presented by Abdolmaleki et al. [40] and Colagrossi and Landrini [20]. The solution obtained with the two-dimensional ANCF analysis is compared to the published numerical and experimental results in Fig. 10. It is clear that all the numerical results agree well. However, in the experimental results, the motion of the water front is slightly slower. The deviation from the experimental results is related in part to experimental uncertainties and partly to some physical effects which are not accounted for in the numerical analysis. At the beginning of the simulation, the departure from the experimental data can be related to imperfections in the initial experimental conditions. In the description of the experimental method, it was reported that it was not possible to record the exact time of the onset of motion, causing the experimental curve to be slightly shifted to the right (further in time) with respect to the numerical solutions. Another shortcoming of the experimental method which causes a delay in the water front motion is the nonuniform breaking of the wax paper. A physical phenomenon, which is not captured by the numerical models and which slows down the fluid front motion, is the turbulence developed at the contact interface between the fluid and the dam (dry deck and side walls). In Fig. 11, the position of the water front obtained with the planar ANCF analysis when a wall is placed at the end of the dam dry deck is compared to the experimental measurements of Martin and Moyce [49] and Lobovský et al. [60]. Overall, a good agreement between the experimental data and the numerical results can be observed. The difference between the experimental results reported in the literature is mainly due to the use of different techniques in the experiments to remove the dam gate [60]. According to the results shown in Fig. 10, neglecting the

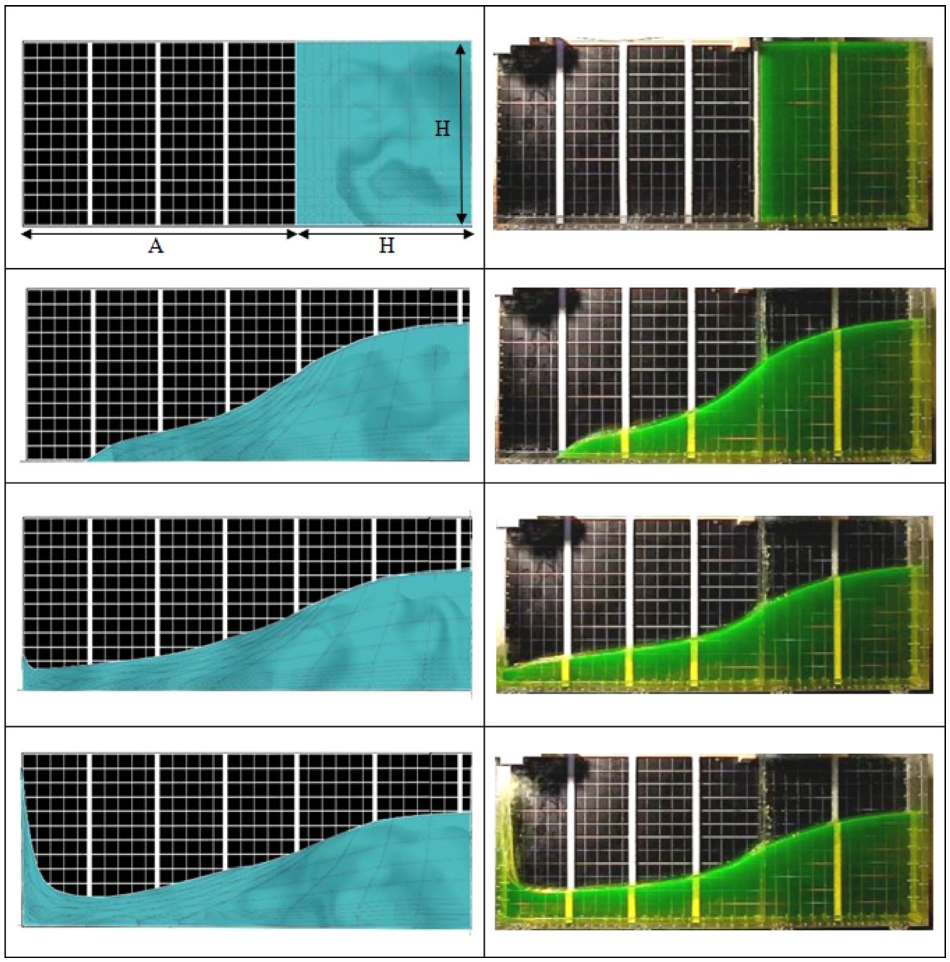

Fig. 8 Comparison between the ANCF planar solution (left) and the experimental results of Lobovský et al. [60] (right). Free surface evolution is measured at times $t^* = 0$, $t^* = 1.27$, $t^* = 1.67$, $t^* = 1.87$ ($H = 600$ mm, $A = 1010$ mm).

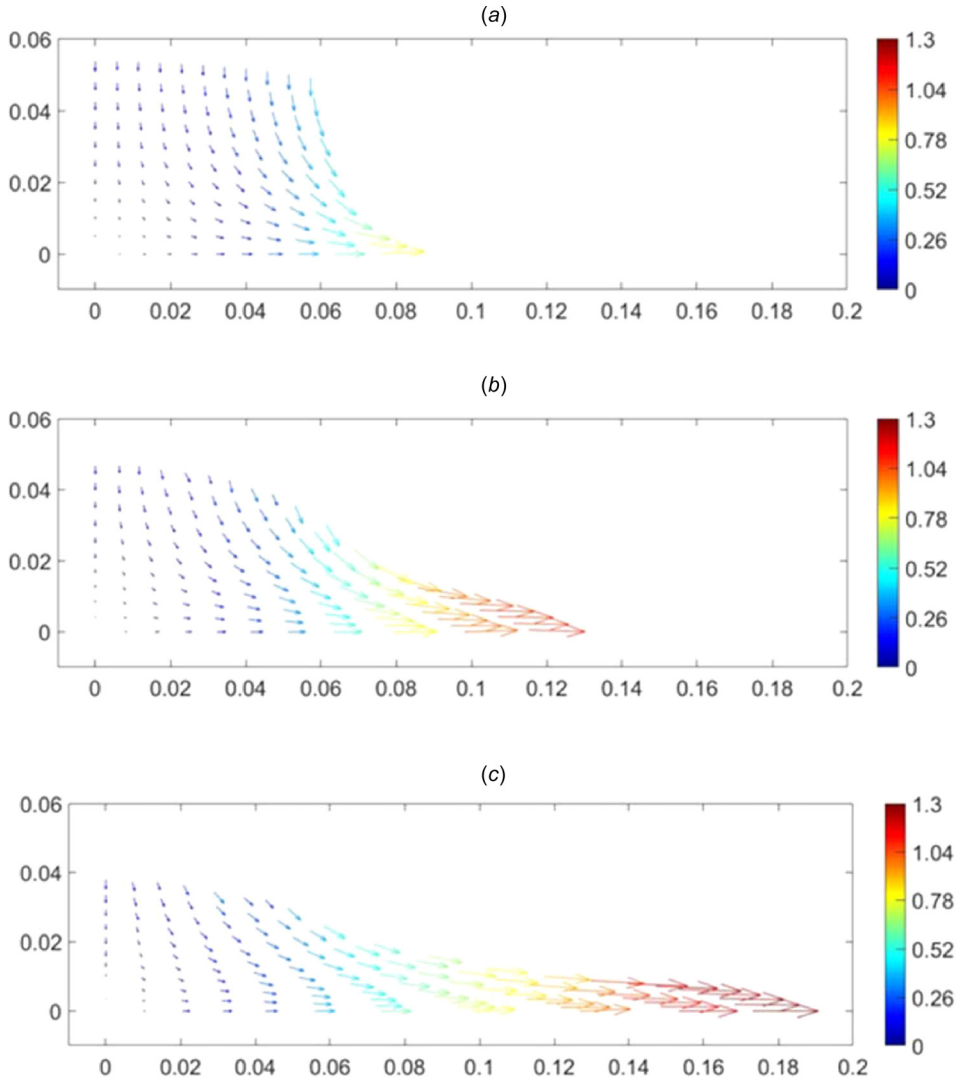

Fig. 9 Velocity field at different times for the broken dam problem using uniform 10×10 rectangular element mesh; velocity is in m/s. (*a*) $t = 0.04$ s, (*b*) $t = 0.08$ s, and (*c*) $t = 0.13$ s.

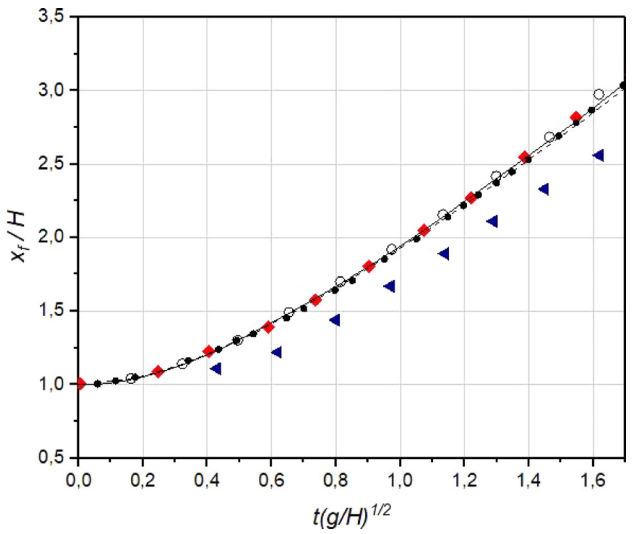

Fig. 10 Water front motion, comparison between two-dimensional ANCF analysis and existing results (◌ Level Set, ◆ BEM, ● SPH, – – – – – – FLUENT, ◀ Experimental, ——— ANCF (100 elements))

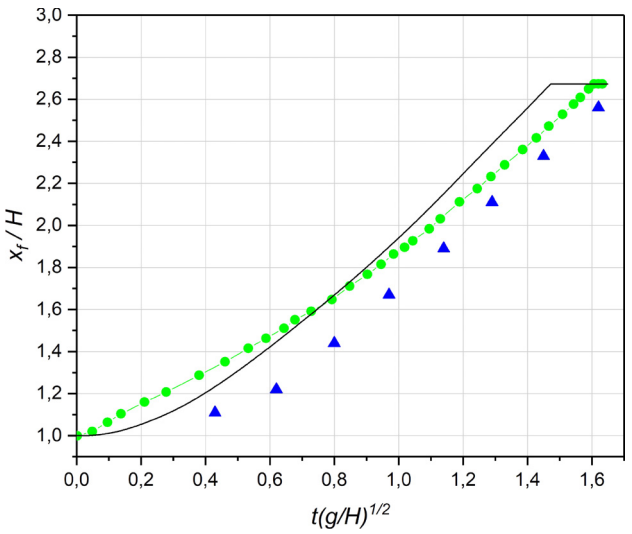

Fig. 11 Surge in the water front motion in case of impact with a wall placed at the end of the dam dry deck (▲ Martin and Moyce [49], —●— from Lobovský et al. [60], ——— ANCF (100 elements))

friction between the fluid and the dam results in a higher velocity of the water front and an earlier impact with the front wall.

7 Three-Dimensional Broken-Dam Flow

For the three-dimensional analysis of the broken dam problem, ANCF brick (solid) elements are used. Each ANCF brick element has eight nodes and is based on an incomplete polynomial representation [66]. These isoparametric high-order elements have been recently used in the analysis of liquid sloshing applications [37–39]. The ANCF brick elements also ensure the continuity of the time-rate of the position vector gradients at the nodal points. Additional continuity conditions can be systematically enforced if desired in order to increase the degree of smoothness and reduce the model dimension. As shown in Appendix B of this paper, the nodal coordinates of element j at node k are defined as

$$\mathbf{e}^j = \begin{bmatrix} \mathbf{r}^{jk^{\mathrm{T}}} & \mathbf{r}_{x1}^{jk^{\mathrm{T}}} & \mathbf{r}_{x2}^{jk^{\mathrm{T}}} & \mathbf{r}_{x3}^{jk^{\mathrm{T}}} \end{bmatrix}^{\mathrm{T}}, \quad k = 1, \ldots, 8 \tag{12}$$

where $\mathbf{r}^{jk}$ is the absolute position vector of node k of finite element j, and $\mathbf{r}_{xl}^{jk}$ is the gradient vector obtained by differentiation with respect to the spatial coordinates x_l, $l = 1, 2, 3$, with $x_1 = x$, $x_2 = y$, and $x_3 = z$. The broken dam problem was solved using uniform $8 \times 8 \times 2$ and $10 \times 10 \times 2$ element mesh models. Only two elements are used to describe the water width, because the fluid deformation in the out-of-plane direction is negligible. Figure 12 shows the progressive collapse of the fluid column as function of time. From the analysis of the results, it is clear that ANCF brick elements can accurately describe the fluid free surface. The position of the water front as function of time and the corresponding velocity field are plotted in Figs. 13 and 14, respectively. Similar to what observed for the two-dimensional case, there is a good agreement between the ANCF solution and the published numerical results.

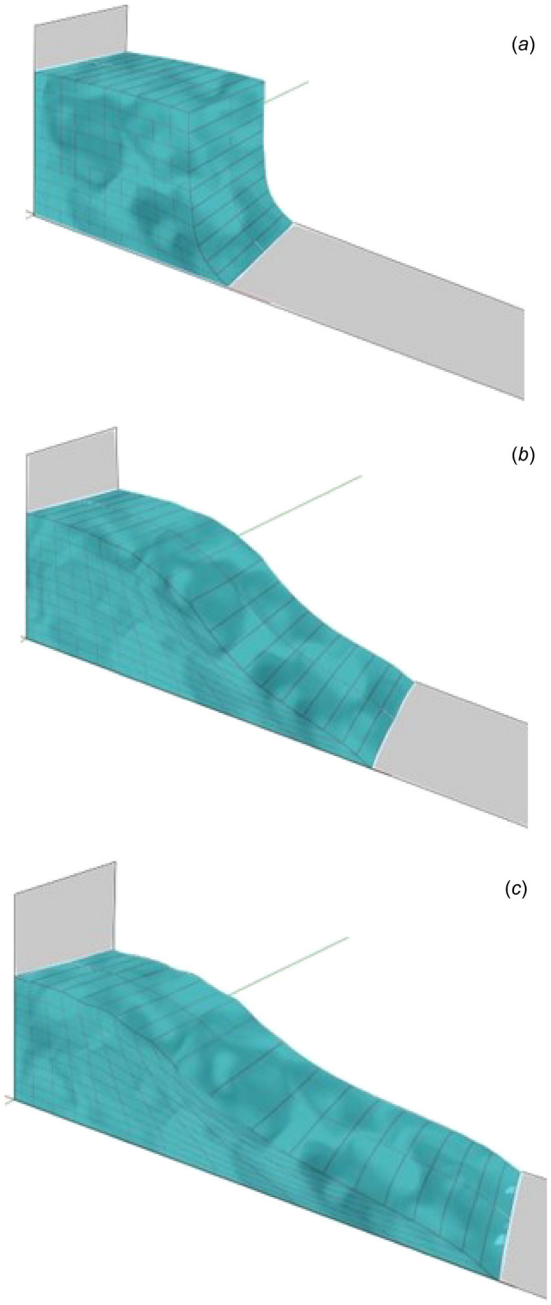

Fig. 12 Free surface profiles for the broken dam problem in three dimensions (10×10×2 elements): (*a*) 0.04 s, (*b*) 0.08 s, and (*c*) 0.10 s

8 Analysis of the Results

In this section, the total Lagrangian ANCF fluid model verified in this paper is evaluated by comparing with the most popular numerical fluid dynamics methods, outlining advantages and limitations. As previously mentioned, fluid–structure interaction problems are currently solved using two main methods: Eulerian and Lagrangian methods. These methods can solve very complex fluid dynamics problems, including turbulent and multiphase flows. Continuum-based total Lagrangian formulations cannot describe the effects of turbulence and air entrapment that characterize multiphase flow problems. Moreover, wave-breaking phenomena and motion of solid bodies through fluids cannot be easily or efficiently analyzed with a continuum-based total Lagrangian approach because of the element distortion. In fluid–structure interaction problems, the fluid dynamic behavior, characterized by large rotations and large deformations, is highly nonlinear. The level of complexity increases considerably if the fluid interacts with multibody systems that represent complex mechanical systems which consist of interconnected rigid and deformable components. In many MBS applications, including liquid sloshing in tanker trucks and freight trains, splashing and turbulence effects can be neglected, because they do not have a significant effect on the overall vehicle dynamics. The main goal in these types of applications is to correctly capture the fluid nominal motion and

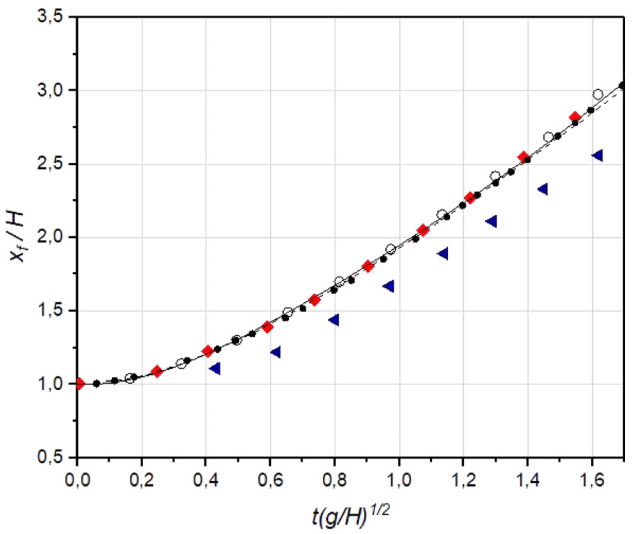

Fig. 13 Water front motion, comparison between three-dimensional ANCF analysis and existing results. (○ Level Set, ◆ BEM, ● SPH, – – – – – – FLUENT, ◀ Experimental, ——— ANCF (10×10×2 elements)).

the highly deformed fluid shape in order to be able to have an accurate estimate of the fluid inertia forces. In these MBS applications, the use of Eulerian-based CFD methods is not straightforward, because most general MBS algorithms are based on total Lagrangian formulations. Using a Lagrangian formulation in the analysis of fluid–structure interaction problems allows using the same field variables for both solids and fluids, thus facilitating the integration with MBS algorithms.

Despite the increase in computing power of modern computers, the high computational cost of mesh-free methods makes them still impractical in many MBS applications. Furthermore, a total Lagrangian continuum-based finite element method employing conventional finite elements cannot be integrated with MBS algorithms since it requires the use of an incremental solution procedure in large rotation problems. This is in addition to the fact that conventional finite elements do not ensure continuity of the strain and stress fields. The ANCF method is a general nonincremental large-rotation and large-deformation finite element formulation which does not impose any restriction on the amount of rotation and deformation within the finite element. This formulation can be systematically integrated with MBS solvers, allowing for the analysis of the interaction between very complex mechanical systems and fluids and for the efficient solution of the liquid sloshing problems in which the turbulence effect on the vehicle dynamics is not significant. Nonetheless, the verification of the results obtained using ANCF finite elements is necessary, and it is the objective of this investigation.

An interesting observation can be made by looking at the data presented in Table 1. This table shows a list of recent papers published on fluid–structure interaction problems, where validation and verification of the numerical solutions is achieved by solving the broken dam problem. In the fluid dynamics literature, different models of the broken dam problem can be found. For this reason, the listed papers have been carefully selected to make sure that

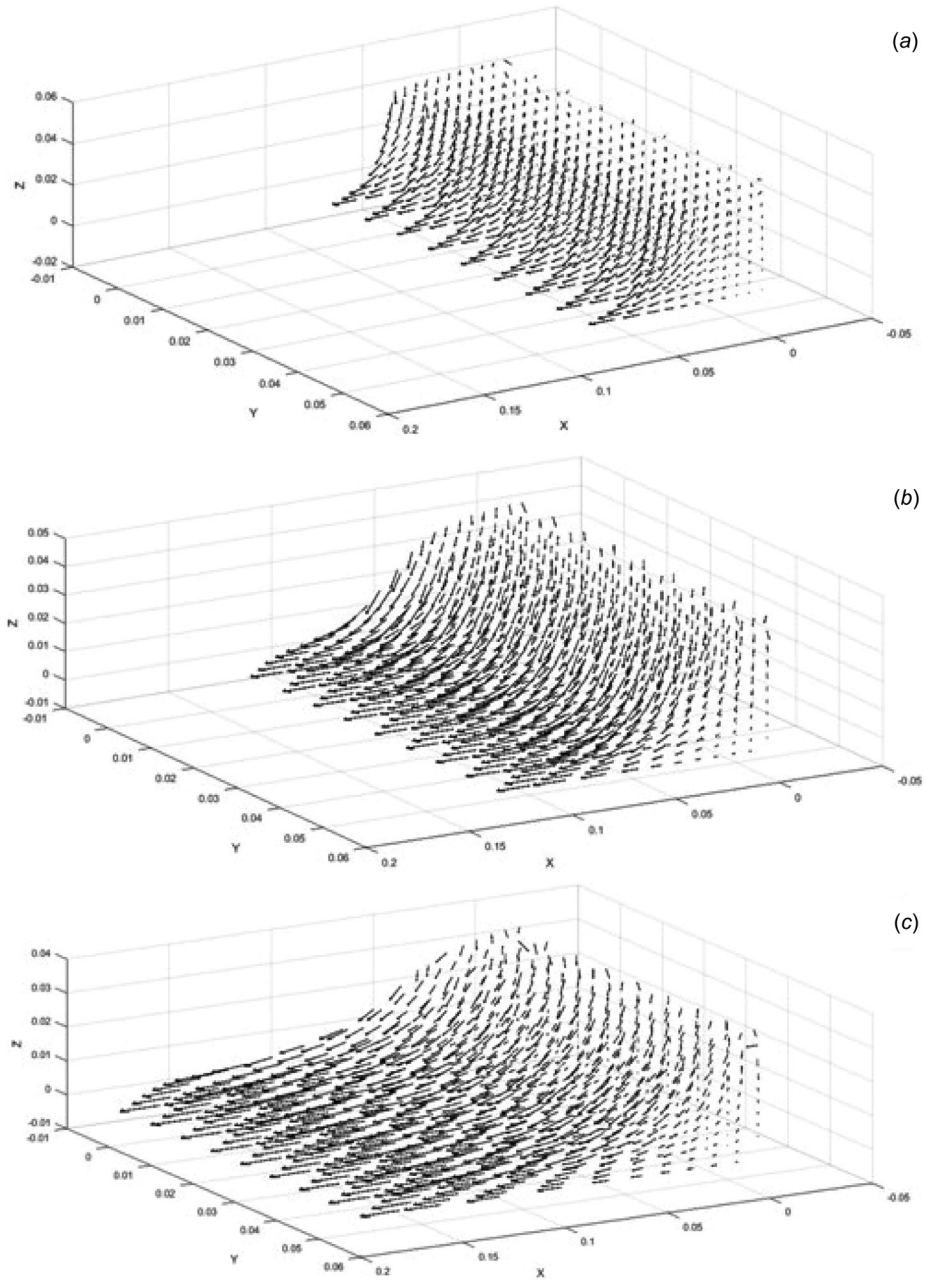

Fig. 14 Velocity field at different time points for the broken dam problem using 10×10×2 solid element mesh: (*a*) $t = 0.04$ s, (*b*) $t = 0.08$ s, and (*c*) $t = 0.13$ s

Table 1 Comparison between different methods

Author	Method	Element	DOF
ANCF (10×10 mesh)	Lagrangian FEM	Quadrilateral ANCF elements	726
Ketabdari and Roozbahani [67]	SPH	—	11,103
Colagrossi and Landrini [20]	SPH	—	12,640
Pathak and Raessi [68]	Eulerian FEM	Quadrilateral element	10,658
Ahn et al. [69]	Eulerian FEM	Quadrilateral element	20,000
Nikseresht et al. [70]	Eulerian FEM	Quadrilateral element	10,302
Ransing et al. [71]	Eulerian FEM	Six-node element	11,940
Cruchaga et al. [72]	Eulerian FEM	Quadrilateral element	11,132
Abdomaleki et al. [40]	Eulerian FVM	Quadrilateral cells	19,642

they all consider the same dam dimensions and same amount of water. The table also shows the solution method and element type used in each paper listed. The number of degrees-of-freedom required to obtain a convergent solution in the case of different methods is presented. It is clear that the number of degrees-of-freedom required for convergence in case of the total Lagrangian ANCF formulation, is around one order of magnitude smaller than what is required by other existing methods. The possibility of reducing the number of degrees-of-freedom allows using a coarser mesh, thus reducing the number of dynamic equations to be solved.

9 Conclusions

This paper is focused on verifying a total Lagrangian continuum-based ANCF fluid dynamics approach for fluid–structure interaction problems. To this end, the results obtained using ANCF finite elements are compared with experimental and numerical results published in the literature for the dam break benchmark problem. The principle of virtual work allows for converting the partial differential equations of motion to a set of second-order ordinary differential equations, which are solved numerically using the HHT numerical integration method. The incompressibility constraint is enforced using a penalty method, and the contact forces between the fluid and the rigid dam are also formulated using a penalty contact formulation. The results of the dam break problem, obtained for two- and three-dimensional cases, are compared with experimental data and with results of other numerical methods, showing a good agreement. The comparison shows that the total Lagrangian formulation that employs ANCF finite elements can accurately capture the fluid free surface large displacement and change in geometry. The fluid deformation resulting from the impact against a wall, placed at the end of the dam dry deck, has also been investigated. The advantages and limitations of the ANCF total Lagrangian approach are discussed. The comparative study presented in this paper shows that the number of degrees-of-freedom required to achieve convergence in the case of the ANCF model is significantly less than the number of degrees-of-freedom required by other methods. Furthermore, the ANCF total Lagrangian fluid approach used in this investigation can be systematically integrated with computational MBS algorithms in order to study sloshing problems in which the effect of turbulence can be neglected.

Acknowledgment

This research was supported by the National Science Foundation (Project No. 1632302).

Appendix A

The two-dimensional ANCF rectangular element, is a four-node element. The nodal coordinates $\mathbf{e}^{jk}$ at the node k of the finite element j can be defined as

$$\mathbf{e}^{jk} = \left[\mathbf{r}^{jk^{\mathrm{T}}}\ \mathbf{r}_x^{jk^{\mathrm{T}}}\ \mathbf{r}_y^{jk^{\mathrm{T}}}\right]^{\mathrm{T}} \quad k = 1, \ldots, 4 \tag{A1}$$

where $\mathbf{r}^{jk}$ is the absolute position vector at the node k of the element j, and $\mathbf{r}_x^{jk}$, $\mathbf{r}_y^{jk}$ are the position vector gradients obtained by differentiation with respect to the spatial coordinates x and y, respectively. The shape functions of the ANCF rectangular element can be derived as follows:

$$\left.\begin{aligned}
S^{1,1} &= -(\xi-1)(\eta-1)(2\eta^2-\eta+2\xi^2-\xi-1),\\
S^{1,2} &= -l\xi(\xi-1)^2(\eta-1), \quad S^{1,3} = -w\eta(\eta-1)^2(\xi-1),\\
S^{2,1} &= \xi(2\eta^2-\eta-3\xi+2\xi^2)(\eta-1),\\
S^{2,2} &= -l\xi^2(\xi-1)(\eta-1), \quad S^{2,3} = w\xi\eta(\eta-1)^2\\
S^{3,1} &= -\xi\eta(1-3\xi-3\eta+2\eta^2+2\xi^2),\\
S^{3,2} &= l\xi^2\eta(\xi-1), \quad S^{3,3} = w\xi\eta^2(\eta-1),\\
S^{4,1} &= \eta(\xi-1)(2\xi^2-\xi-3\eta+2\eta^2),\\
S^{4,2} &= l\xi\eta(\xi-1)^2, \quad S^{4,3} = -w\eta^2(\xi-1)(\eta-1)
\end{aligned}\right\} \tag{A2}$$

where l and w are, respectively, the dimensions of the element along the axes x and y,$\xi = x/l$, $\eta = y/w$, and ξ, and $\eta \in [0, 1]$. The position vector of an arbitrary material point on element j can be written as

$$\mathbf{r}^j = \sum_{k=1}^{4} [S^{k,1}\mathbf{I}\ S^{k,2}\mathbf{I}\ S^{k,3}\mathbf{I}]\mathbf{e}^{jk} = \mathbf{S}^j\mathbf{e}^j \tag{A3}$$

where $\mathbf{I}$ is the 2×2 identity matrix, $\mathbf{S}^j$ and $\mathbf{e}^j$ are, respectively, the element shape function matrix and the vector of nodal coordinates which can be written as

$$\left.\begin{aligned}
\mathbf{S}^j &= [S^{1,1}\mathbf{I}\ S^{1,2}\mathbf{I}\ S^{1,3}\mathbf{I}\ \cdots\ S^{4,1}\mathbf{I}\ S^{4,2}\mathbf{I}\ S^{4,3}\mathbf{I}]\\
\mathbf{e}^j &= [\mathbf{e}^{j1^{\mathrm{T}}}\ \mathbf{e}^{j2^{\mathrm{T}}}\ \mathbf{e}^{j3^{\mathrm{T}}}\ \mathbf{e}^{j4^{\mathrm{T}}}]^{\mathrm{T}}
\end{aligned}\right\} \tag{A4}$$

Appendix B

The three-dimensional ANCF solid element, with an incomplete polynomial representation, used in this investigation is an eight-node element. The nodal coordinates $\mathbf{e}^{jk}$ at the node k of the finite element j can be defined as

$$\mathbf{e}^{jk} = \left[\mathbf{r}^{jk^{\mathrm{T}}}\ \mathbf{r}_x^{jk^{\mathrm{T}}}\ \mathbf{r}_y^{jk^{\mathrm{T}}}\ \mathbf{r}_z^{jk^{\mathrm{T}}}\right]^{\mathrm{T}} \quad k = 1, \ldots, 8 \tag{B1}$$

where $\mathbf{r}^{jk}$ is the absolute position vector at the node k of the element j, and $\mathbf{r}_x^{jk}$, $\mathbf{r}_y^{jk}$, and $\mathbf{r}_z^{jk}$ are the position vector gradients obtained by differentiation with respect to the spatial coordinates

$x, y,$ and z, respectively. The displacement field of each position coordinate of the solid fluid element can be defined using an incomplete polynomial with 32 coefficients as

$$\begin{aligned}\phi(x,y,z) = {} & \alpha_1 + \alpha_2 x + \alpha_3 y + \alpha_4 z + \alpha_5 x^2 \\ & + \alpha_6 y^2 + \alpha_7 z^2 + \alpha_8 xy + \alpha_9 yz + \alpha_{10} xz \\ & + \alpha_{11} x^3 + \alpha_{12} y^3 + \alpha_{13} z^3 + \alpha_{14} x^2 y \\ & + \alpha_{15} x^2 z + \alpha_{16} y^2 z + \alpha_{17} xy^2 + \alpha_{18} xz^2 + \alpha_{19} yz^2 \\ & + \alpha_{20} xyz + \alpha_{21} x^3 y + \alpha_{22} x^3 z + \alpha_{23} xy^3 \\ & + \alpha_{24} y^3 z + \alpha_{25} xz^3 + \alpha_{26} yz^3 + \alpha_{27} x^2 yz \\ & + \alpha_{28} xy^2 z + \alpha_{29} xyz^2 + \alpha_{30} x^3 yz + \alpha_{31} xy^3 z + \alpha_{32} xyz^3 \end{aligned} \tag{B2}$$

In this equation, α_k, $k = 1, 2, \ldots, 32$, are the polynomial coefficients. Using this polynomial description, the shape functions of the ANCF brick element can be derived as follows:

$$\left.\begin{aligned} S^{k,1} &= (-1)^{1+\xi_k+\eta_k+\zeta_k}(\xi+\xi_k-1)(\eta+\eta_k-1)(\zeta+\zeta_k-1)\cdot \\ &(1+(\xi-\xi_k)(1-2\xi)+(\eta-\eta_k)(1-2\eta)+(\zeta-\zeta_k)(1-2\zeta)) \\ S^{k,2} &= (-1)^{\eta_k+\zeta_k} a \xi^{\xi_k+1}(\xi-1)^{2-\xi_k}\eta^{\eta_k}(\eta-1)^{1-\eta_k}\zeta^{\zeta_k}(\zeta-1)^{1-\zeta_k} \\ S^{k,3} &= (-1)^{\xi_k+\zeta_k} b \xi^{\xi_k}(\xi-1)^{1-\xi_k}\eta^{\eta_k+1}(\eta-1)^{2-\eta_k}\zeta^{\zeta_k}(\zeta-1)^{1-\zeta_k} \\ S^{k,4} &= (-1)^{\xi_k+\eta_k} c \xi^{\xi_k}(\xi-1)^{1-\xi_k}\eta^{\eta_k}(\eta-1)^{1-\eta_k}\zeta^{\zeta_k+1}(\zeta-1)^{2-\zeta_k} \\ & k = 1, 2, \ldots, 8 \end{aligned}\right\} \tag{B3}$$

where $a, b,$ and c are, respectively, the dimensions of the element along the axes $x, y,$ and z directions, $\xi = x/a,\ \eta = y/b,\ \zeta = z/c$, $\xi,\ \eta,\ \zeta \in [0, 1]$, and ξ_k, η_k, ζ_k are the dimensionless nodal locations for node k. The position vector of an arbitrary material point on element j can be written as

$$\mathbf{r}^j = \sum_{k=1}^{8} [S^{k,1}\mathbf{I}\ S^{k,2}\mathbf{I}\ S^{k,3}\mathbf{I}\ S^{k,4}\mathbf{I}]\mathbf{e}^{jk} = \mathbf{S}^j\mathbf{e}^j \tag{B4}$$

where $\mathbf{I}$ is the 3×3 identity matrix, $\mathbf{S}^j$ and $\mathbf{e}^j$ are, respectively, the element shape function matrix and the vector of nodal coordinates which can be written as

$$\left.\begin{aligned} \mathbf{S}^j &= [S^{1,1}\mathbf{I}\ S^{1,2}\mathbf{I}\ S^{1,3}\mathbf{I}\ S^{1,4}\mathbf{I}\ \cdots\ S^{8,1}\mathbf{I}\ S^{8,2}\mathbf{I}\ S^{8,3}\mathbf{I}\ S^{8,4}\mathbf{I}] \\ \mathbf{e}^j &= [\mathbf{e}^{j1^{\mathrm{T}}}\ \mathbf{e}^{j2^{\mathrm{T}}}\ \mathbf{e}^{j3^{\mathrm{T}}}\ \mathbf{e}^{j4^{\mathrm{T}}}\ \mathbf{e}^{j5^{\mathrm{T}}}\ \mathbf{e}^{j6^{\mathrm{T}}}\ \mathbf{e}^{j7^{\mathrm{T}}}\ \mathbf{e}^{j8^{\mathrm{T}}}]^T \end{aligned}\right\} \tag{B5}$$

References

[1] Donea, J., and Huerta, A., 2003, *Finite Element Methods for Flow Problems*, Wiley, Chichester, UK.

[2] Chan, R. K. C., and Street, R. L., 1970, "A Computer Study of Finite-Amplitude Water Waves," J. Comput. Phys., **6**(1), pp. 68–94.

[3] Harlow, F. H., and Welch, J. E., 1965, "Numerical Calculation of Time-Dependent Viscous Incompressible Flow of Fluid With Free Surface," Phys. Fluids, **8**(12), pp. 2182–2189.

[4] Hirt, C. W., and Cook, J. L., 1972, "Calculating Three-Dimensional Flows Around Structures and Over Rough Terrain," J. Comput. Phys., **10**(2), pp. 324–340.

[5] Ramshaw, J. D., and Trapp, J. A., 1976, "A Numerical Technique for Low-Speed Homogeneous Two-Phase Flow With Sharp Interfaces," J. Comput. Phys., **21**(4), pp. 438–453.

[6] Nakayama, T., and Mori, M., 1996, "An Eulerian Finite Element Method for Time-Dependent Free Surface Problems in Hydrodynamics," Int. J. Numer. Methods Fluids, **22**(3), pp. 175–194.

[7] Hirt, C. W., and Nichols, B. D., 1981, "Volume of Fluid (VOF) Method for the Dynamics of Free Boundaries," J. Comput. Phys., **39**(1), pp. 201–225.

[8] Kim, M. S., and Lee, W. I., 2003, "A New VOF-Based Numerical Scheme for the Simulation of Fluid Flow With Free Surface—Part I: New Free Surface-Tracking Algorithm and Its Verification," Int. J. Numer. Methods Fluids, **42**(7), pp. 765–790.

[9] Rider, W. J., and Kothe, D. B., 1998, "Reconstructing Volume Tracking," J. Comput. Phys., **141**(2), pp. 112–152.

[10] Rudman, M., 1997, "Volume-Tracking Methods for Interfacial Flow Calculations," Int. J. Numer. Methods Fluids, **24**(7), pp. 671–691.

[11] Soo Kim, M., Sun Park, J., and Lee, W. I., 2003, "A New VOF-Based Numerical Scheme for the Simulation of Fluid Flow With Free Surface—Part II: Application to the Cavity Filling and Sloshing Problems," Int. J. Numer. Methods Fluids, **42**(7), pp. 791–812.

[12] Viecelli, J. A., 1969, "A Method for Including Arbitrary External Boundaries in the MAC Incompressible Fluid Computing Technique," J. Comput. Phys., **4**(4), pp. 543–551.

[13] Hirt, C. W., Amsden, A. A., and Cook, J. L., 1997, "An Arbitrary Lagrangian–Eulerian Computing Method for All Flow Speeds," J. Comput. Phys., **135**(2), pp. 203–216.

[14] Hughes, T. J., Liu, W. K., and Zimmermann, T. K., 1981, "Lagrangian-Eulerian Finite Element Formulation for Incompressible Viscous Flows," Comput. Methods Appl. Mech. Eng., **29**(3), pp. 329–349.

[15] Navti, S. E., Ravindran, K., Taylor, C., and Lewis, R. W., 1997, "Finite Element Modelling of Surface Tension Effects Using a Lagrangian-Eulerian Kinematic Description," Comput. Methods Appl. Mech. Eng., **147**(1–2), pp. 41–60.

[16] Oñate, E., and García, J., 2001, "A Finite Element Method for Fluid–Structure Interaction With Surface Waves Using a Finite Calculus Formulation," Comput. Methods Appl. Mech. Eng., **191**(6–7), pp. 635–660.

[17] Soulaimani, A., and Saad, Y., 1998, "An Arbitrary Lagrangian-Eulerian Finite Element Method for Solving Three-Dimensional Free Surface Flows," Comput. Methods Appl. Mech. Eng., **162**(1–4), pp. 79–106.

[18] Belytschko, T., Liu, W. K., Moran, B., and Elkhodary, K., 2013, *Nonlinear Finite Elements for Continua and Structures*, Wiley, New York.

[19] Adami, S., Hu, X. Y., and Adams, N. A., 2012, "A Generalized Wall Boundary Condition for Smoothed Particle Hydrodynamics," J. Comput. Phys., **231**(21), pp. 7057–7075.

[20] Colagrossi, A., and Landrini, M., 2003, "Numerical Simulation of Interfacial Flows by Smoothed Particle Hydrodynamics," J. Comput. Phys., **191**(2), pp. 448–475.

[21] Colagrossi, A., 2005, "A Meshless Lagrangian Method for Free–Surface and Interface Flows With Fragmentation," Ph.D. thesis, Università di Roma, Rome, Italy.

[22] González, D., Cueto, E., Chinesta, F., and Doblaré, M., 2007, "A Natural Element Updated Lagrangian Strategy for Free-Surface Fluid Dynamics," J. Comput. Phys., **223**(1), pp. 127–150.

[23] Kondo, M., and Koshizuka, S., 2011, "Improvement of Stability in Moving Particle Semi-Implicit Method," Int. J. Numer. Methods Fluids, **65**(6), pp. 638–654.

[24] Monaghan, J. J., and Gingold, R. A., 1983, "Shock Simulation by the Particle Method SPH," J. Comput. Phys., **52**(2), pp. 374–389.

[25] Monaghan, J. J., and Kocharyan, A., 1995, "SPH Simulation of Multi-Phase Flow," Comput. Phys. Commun., **87**(1–2), pp. 225–235.

[26] Monaghan, J. J., and Kos, A., 1999, "Solitary Waves on a Cretan Beach," J. Waterw., Port, Coastal, Ocean Eng., **125**(3), pp. 145–155.

[27] Monaghan, J. J., 1988, "An Introduction to SPH," Comput. Phys. Commun., **48**(1), pp. 89–96.

[28] Monaghan, J. J., 1992, "Smoothed Particle Hydrodynamics," Annu. Rev. Astron. Astrophys., **30**(1), pp. 543–574.

[29] Monaghan, J. J., 1994, "Simulating Free Surface Flows With SPH," J. Comput. Phys., **110**(2), pp. 399–406.

[30] Monaghan, J. J., Cas, R. A. F., Kos, A. M., and Hallworth, M., 1999, "Gravity Currents Descending a Ramp in a Stratified Tank," J. Fluid Mech., **379**, pp. 39–69.

[31] Shao, S., and Lo, E. Y., 2003, "Incompressible SPH Method for Simulating Newtonian and Non-Newtonian Flows With a Free Surface," Adv. Water Resour., **26**(7), pp. 787–800.

[32] Nayroles, B., Touzot, G., and Villon, P., 1992, "Generalizing the Finite Element Method: Diffuse Approximation and Diffuse Elements," Comput. Mech., **10**(5), pp. 307–318.

[33] Pape, D., Thornton, B., and Yugulis, K., 2016, "Slosh Characteristics of Aggregated Intermediate Bulk Containers on Single-Unit Trucks," *Federal Motor Carrier Safety Administration*, U.S. Department of Transportation, Washington, DC.

[34] Cheli, F., D'Alessandro, V., Premoli, A., and Sabbioni, E., 2013, "Simulation of Sloshing in Tank Trucks," Int. J. Heavy Veh. Syst., **20**(1), pp. 1–18.

[35] Elliott, A. S., Slattengren, J., and Buijk, A., 2006, "Fully Coupled Fluid/Mechanical Response Prediction for Truck-Mounted Tank Sloshing Using Cosimulation of MSC.ADAMS® and MSC.Dytran®," SAE Paper No. 2006-01-0932.

[36] Barton, M. S., Corson, D., Quigley, J., Emami, B., and Kush, T., 2014, "Tanker Truck Sloshing Simulation Using Bi-Directionally Coupled CFD and Multi-Body Dynamics Solvers," SAE Paper No. 2014-01-2442.

[37] Wei, C., Wang, L., and Shabana, A. A., 2015, "A Total Lagrangian ANCF Liquid Sloshing Approach for Multibody System Applications," ASME J. Comput. Nonlinear Dyn., **10**(5), p. 051014.

[38] Shi, H., Wang, L., Nicolsen, B., and Shabana, A. A., 2017, "Integration of Geometry and Analysis for the Study of Liquid Sloshing in Railroad Vehicle Dynamics," Proc. Inst. Mech. Eng., Part K: J. Multi-Body Dyn., **231**(4), pp. 608–629.

[39] Nicolsen, B., Wang, L., and Shabana, A., 2017, "Nonlinear Finite Element Analysis of Liquid Sloshing in Complex Vehicle Motion Scenarios," J. Sound Vib., **405**, pp. 208–233.
[40] Abdolmaleki, K., Thiagarajan, K. P., and Morris-Thomas, M. T., 2004, "Simulation of the Dam Break Problem and Impact Flows Using a Navier–Stokes Solver," Simulations, **13**, p. 17.
[41] Brufau, P., and Garcia-Navarro, P., 2000, "Two-Dimensional Dam Break Flow Simulation," Int. J. Numer. Methods Fluids, **33**(1), pp. 35–57.
[42] Huerta, A., and Liu, W. K., 1988, "Viscous Flow With Large Free Surface Motion," Comput. Methods Appl. Mech. Eng., **69**(3), pp. 277–324.
[43] Korobkin, A., and Yilmaz, O., 2009, "The Initial Stage of Dam-Break Flow," J. Eng. Math., **63**(2–4), pp. 293–308.
[44] Rakhsha, M., Pazouki, A., and Negrut, D., 2016, "Incompressible Implicit SPH," Technical Report No. TR03.
[45] Rumold, W., 2001, "Modeling and Simulation of Vehicles Carrying Liquid Cargo," Multibody Syst. Dyn., **5**(4), pp. 351–374.
[46] Shin, S., and Lee, W. I., 2000, "Finite Element Analysis of Incompressible Viscous Flow With Moving Free Surface by Selective Volume of Fluid Method," Int. J. Heat Fluid Flow, **21**(2), pp. 197–206.
[47] Stansby, P. K., Chegini, A., and Barnes, T. C. D., 1998, "The Initial Stages of Dam-Break Flow," J. Fluid Mech., **374**, pp. 407–424.
[48] Wang, S. P., and Wang, K. K., 1994, "A Net Inflow Method for Incompressible Viscous Flow With Moving Free Surface," Int. J. Numer. Methods Fluids, **18**(7), pp. 669–694.
[49] Martin, J. C., and Moyce, W. J., 1952, "Part IV—An Experimental Study of the Collapse of Liquid Columns on a Rigid Horizontal Plane," Philos. Trans. R. Soc. London A: Math., Phys. Eng. Sci., **244**(882), pp. 312–324.
[50] Shabana, A. A., 2017, *Computational Continuum Mechanics*, 3rd ed., Wiley, Chichester, UK.
[51] Langtangen, H. P., Mardal, K. A., and Winther, R., 2002, "Numerical Methods for Incompressible Viscous Flow," Adv. Water Resour., **25**(8), pp. 1125–1146.
[52] González, J. A., Lee, Y. S., and Park, K. C., 2017, "Stabilized Mixed Displacement–Pressure Finite Element Formulation for Linear Hydrodynamic Problems With Free Surfaces," Comput. Methods Appl. Mech. Eng., **319**, pp. 314–337.
[53] Kim, N. H., 2014, *Introduction to Nonlinear Finite Element Analysis*, Springer Science & Business Media, New York.
[54] Jun, L., 1988, "Numerical Simulation of Flow With Moving Interface," PhysicoChemical Hydrodyn., **10**(5), p. 625.
[55] Okamoto, T., and Kawahara, M., 1990, "Two-Dimensional Sloshing Analysis by Lagrangian Finite Element Method," Int. J. Numer. Methods Fluids, **11**(5), pp. 453–477.
[56] Ramaswamy, B., Kawahara, M., and Nakayama, T., 1986, "Lagrangian Finite Element Method for the Analysis of Two-Dimensional Sloshing Problems," Int. J. Numer. Methods Fluids, **6**(9), pp. 659–670.
[57] Sung, J., Choi, H. G., and Yoo, J. Y., 1999, "Finite Element Simulation of Thin Liquid Film Flow and Heat Transfer Including a Hydraulic Jump," Int. J. Numer. Methods Eng., **46**(1), pp. 83–101.
[58] Shabana, A. A., Zaazaa, K. E., and Sugiyama, H., 2008, *Railroad Vehicle Dynamics: A Computational Approach*, CRC, Boca Raton, FL.
[59] Olshevskiy, A., Dmitrochenko, O., and Kim, C., 2013, "Three- and Four-Noded Planar Elements Using Absolute Nodal Coordinate Formulation," Multibody Syst. Dyn., **29**(3), pp. 255–269.
[60] Lobovský, L., Botia-Vera, E., Castellana, F., Mas-Soler, J., and Souto-Iglesias, A., 2014, "Experimental Investigation of Dynamic Pressure Loads During Dam Break," J. Fluids Struct., **48**, pp. 407–434.
[61] Osher, S., and Sethian, J. A., 1988, "Fronts Propagating With Curvature-Dependent Speed: Algorithms Based on Hamilton-Jacobi Formulations," J. Comput. Phys., **79**(1), pp. 12–49.
[62] López-Villa, A., Zamudio, L. S., and Medina, A., 2014, "The Boundary Element Method in Fluid Mechanics: Application to Bubble Growth," *Experimental and Computational Fluid Mechanics*, Springer International Publishing, Cham, Switzerland, pp. 17–48.
[63] McDonald, P. W., 1971, "The Computation of Transonic Flow Through Two-Dimensional Gas Turbine Cascades," ASME Paper No. 71-GT-89.
[64] MacCormack, R., and Paullay, A., 1972, "Computational Efficiency Achieved by Time Splitting of Finite Difference Operators," AIAA Paper No. 72-154.
[65] FLUENT, 2001, *FLUENT 6 User's Guide*, Fluent Inc., Canonsburg, PA.
[66] Olshevskiy, A., Dmitrochenko, O., and Kim, C. W., 2013, "Three-Dimensional Solid Brick Element Using Slopes in the Absolute Nodal Coordinate Formulation," ASME J. Comput. Nonlinear Dyn., **9**(2), p. 021001.
[67] Ketabdari, M. J., and Roozbahani, A. N., 2013, "Numerical Simulation of Plunging Wave Breaking by the Weakly Compressible Smoothed Particle Hydrodynamic Method," J. Appl. Mech. Tech. Phys., **54**(3), pp. 477–486.
[68] Pathak, A., and Raessi, M., 2016, "A 3D, Fully Eulerian, VOF-Based Solver to Study the Interaction Between Two Fluids and Moving Rigid Bodies Using the Fictitious Domain Method," J. Comput. Phys., **311**, pp. 87–113.
[69] Ahn, H. T., Shashkov, M., and Christon, M. A., 2009, "The Moment-of-Fluid Method in Action," Int. J. Numer. Methods Biomed. Eng., **25**(10), pp. 1009–1018.
[70] Nikseresht, A. H., Alishahi, M. M., and Emdad, H., 2005, "Volume-of-Fluid Interface Tracking With Lagrangian Propagation for Incompressible Free Surface Flows," Sci. Iran., **12**(2), pp. 131–140.
[71] Ransing, R. S., Savino, S., and Lewis, R. W., 2005, "Numerical Optimization of Tilt Casting Process," Int. J. Cast Met. Res., **18**(2), pp. 109–118.
[72] Cruchaga, M. A., Celentano, D. J., and Tezduyar, T. E., 2005, "Moving-Interface Computations With the Edge-Tracked Interface Locator Technique (ETILT)," Int. J. Numer. Methods Fluids, **47**(6–7), pp. 451–469.